

Self Calibration and Analysis of the Surphaser 25HS 3D Scanner

Derek LICHTI, Australia, Stefan BRÜSTLE, Germany and Jochen FRANKE, Australia

Key words: laser scanner, calibration, systematic error

SUMMARY

In this paper we present a detailed analysis of the results from a self-calibration experiment conducted on the Surphaser Hemispherical 3D Scanner 25HS terrestrial laser scanner, which offers a full horizontal field of view (FOV) and 270° vertical FOV. The CW rangefinder's central wavelength is 690 nm and features very high precision, with manufacturer-claimed 1-sigma distance noise estimates at 10 m of 0.1 mm and 0.3 mm for 80% and 20% reflectivity, respectively. Angular precision is quoted at 15" in both the horizontal and vertical directions. Eight scans of an indoor, 3D network of signalised points were captured from different locations. After describing the instrument specifications and the experiment in more detail, a method developed to pre-process the intensity data to correct its significant drop-off as a function of range is explained. The circular target measurement algorithm developed is then discussed, followed by the observation equations and adjustment model and detailed analyses of the self-calibration results. The results indicate the existence of small but statistically significant systematic errors in the rangefinder and elevation angle measurements. In addition, evidence of mass imbalance of the system exists in the calibration adjustment results.

Self Calibration and Analysis of the Surphaser 25HS 3D Scanner

Derek LICHTI, Australia, Stefan BRÜSTLE, Germany and Jochen FRANKE, Australia

1. INTRODUCTION

The number of commercially-available amplitude-modulated continuous-wave (AM-CW) terrestrial laser scanners (TLSs) has increased considerably in the past few years. Examples include the Faro LS 840 and LS 880, the Zoller+Fröhlich IMAGER 5006, the Surphaser Hemispherical 3D Scanner 25HS/HSX and the Callidus CPW 8000, which combines both AM-CW and pulse rangefinding technologies. Generally speaking, AM-CW instruments offer accurate, unambiguous range measurements up to several tens of metres (i.e. < 100 m). However, their principal advantage over scanners using the pulse method is the speed of data acquisition, which on the order of hundreds of thousands of points per second. Pulse method instruments are by comparison quite slower.

Several researchers have reported on the performance and calibration of AM-CW laser scanners. Amiri Parian and Grün (2005) report on the self-calibration of the Z+F Imager 5003. They use 2D image point observations derived from the scanner data in an extended panoramic camera model but only model angular systematic errors, not rangefinder errors. Abmayr et al. (2005) address calibration of the Z+F Imager 5003 with error models originating from theodolite modelling. They propose a simple, non-simultaneous calibration method for estimating trunnion axis error, collimation axis error and vertical circle index error. Lichti (2007) reports on a series of calibrations of a Faro 880 laser scanner. Also noteworthy is Reshetyuk (2006) who reports on the calibration of two pulse-method scanners.

This paper reports on an investigation into the self-calibration of the Surphaser Hemispherical 3D Scanner 25HS. First, some of the salient properties of the instrument are presented and discussed. The data acquisition procedure, which was similar to that used for tests performed on the Faro 880 by the first author, is then described. The intensity data processing that was needed prior to calibration is then detailed. This is followed by the relevant mathematical models, self-calibration adjustment results and analyses. Concluding remarks complete the paper

2. EXPERIMENT DESCRIPTION

2.1 The Surphaser Scanner

Pictured in Figure 1, the Surphaser Hemispherical 3D Scanner 25HS offers a full horizontal field of view (FOV) and 270° vertical FOV. The AM-CW rangefinder has a central wavelength of 690 nm and features high precision range measurements. The manufacturer's claimed 1σ precision distance noise estimates at 10 m are 0.1 mm and 0.3 mm for 80% and 20% reflectivity, respectively. The optimal effective range for the instrument is specified at 1.5 m to 22 m. The scanner's angular precision is quoted at 15" for both the horizontal and

vertical angles. Its maximum horizontal and vertical resolutions are 80 points/° and its data capture rate is 190 kHz. More details can be found at the Surphaser website (Basis Software, 2007).



Figure 1. Surphaser Hemispherical 3D Scanner 25HS. Image courtesy of Basis Software (2007).

2.2 Data Acquisition

A similar self-calibration procedure that has been used successfully in the past (e.g., Lichti 2007) was adopted to test the Surphaser scanner. One hundred A3-size, circular paper targets were mounted on the walls, floor and ceiling of a room measuring 12.5 m x 7.0 m x 2.6 m. Eight scans were captured from two different locations (4 per location), with each differing in terms of κ rotation angle by 90°. The rotation was accomplished by lifting the entire tripod assembly after each dataset was captured. The instrument was levelled with a bull's eye bubble for each scan except for the first. The two nominal locations were in opposing corners of the room and at least 1.3 m from the nearest wall. The angular sampling interval of the scans was approximately 0.057°.

Data for each scan were captured throughout the instrument's full horizontal and vertical fields of view. Unfortunately, though, proprietary Surphaser processing software truncated the data, which meant loss of the lower 12° from the vertical FOV. Though this was not ideal, it was not considered to be of great concern in terms of compromising geometric strength thanks to the very high redundancy of the calibration network design.

Returning to the targets, proprietary Faro targets were used since they were readily available to the authors. Pictured in Figure 2, these consist of a white circle (200 mm diameter for the A3 size) on a grey background. However, the proprietary Faro contrast-centroiding algorithm

used for Faro scanner evaluations (e.g. Lichti, 2007) was not used for target centre co-ordinate measurement here. Instead, a specially-designed algorithm was used and will be described later.

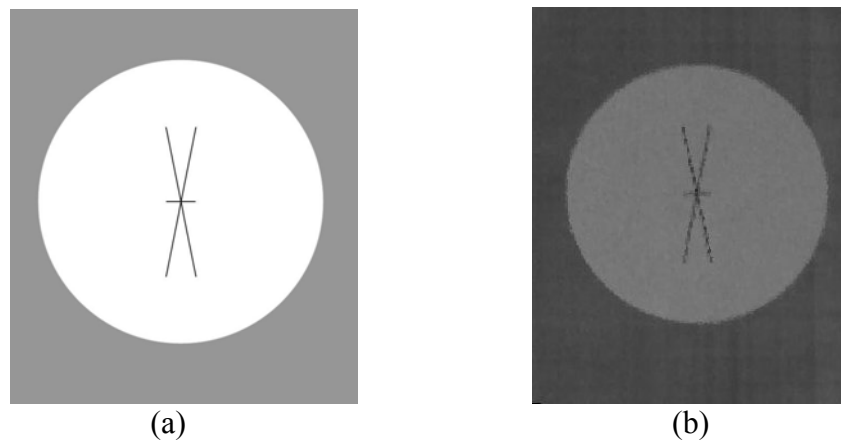


Figure 2. Faro target a) template and b) appearance in a Surphaser point cloud.

2.3 Data Pre-Processing

A test scan was captured prior to calibration data acquisition in order for the operator to select the appropriate a priori brightness settings. In spite of this, radiometric correction of the intensity was necessary in order to make the data useful. A significant drop-off in return signal intensity existed in the data, particularly at longer ranges. Targets at the end opposite end of the room from where the scanner was located captured were not visible in the data, so some form of contrast stretch was required. Both linear and histogram equalisation methods were tested but both proved to be inadequate at all ranges. A sigmoid-type function of the following form was therefore used:

$$e'_i = A \{2 + \sin[b\pi(\rho - \rho_0)]\} \quad (1)$$

where, e and e' are the original and corrected intensities, respectively, of a particular point i , ρ is the range to point i , and A , b and ρ_0 are empirical constants derived from the statistics of each point cloud. Figure 3 shows an example point cloud before and Figure 4 shows the point cloud after the sigmoid intensity correction, which was clearly effective.

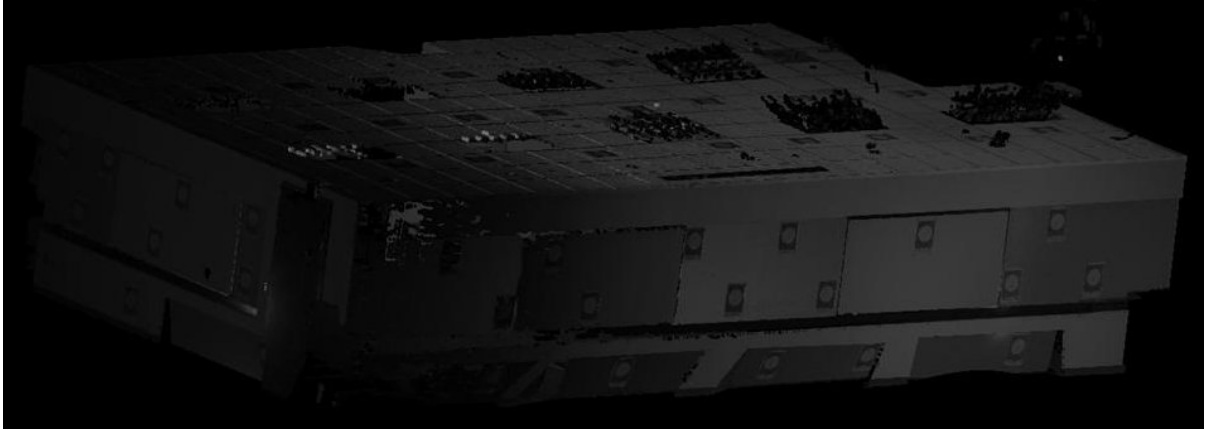


Figure 3. Point cloud before intensity correction.

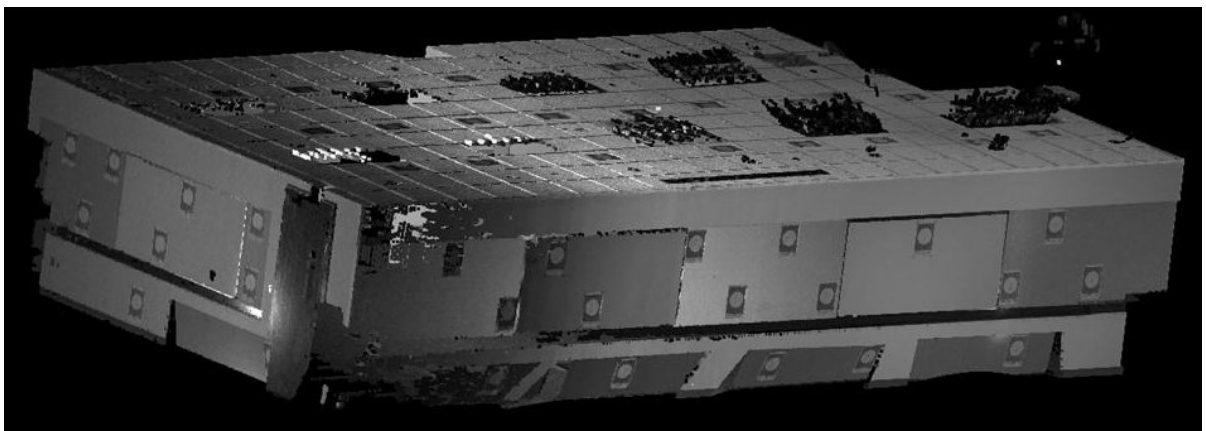


Figure 4. Point cloud after intensity correction.

2.4 Target Measurement

Software for semi-automatic target centre co-ordinate measurement for the Surphaser testing was built by the first author. First, the user picks the approximate target centre (the seed point) from a resampled (but lower resolution) 2D intensity image, an example of which is pictured in Figure 5. A subset of points neighbouring this seed point is then extracted from the original 3D point cloud. The number of points depends on the target range, but can be easily calculated knowing the target dimensions and angular sampling interval of the scanner. The area spanned by the neighbourhood subset should be larger than the circular portion of the target.



Figure 5. Two-dimensional point cloud view for target measurement.

Precise measurement of the target centre co-ordinates is done in two steps. First, the best-fit plane of target subset points is determined by orthogonal regression (Shakarji, 1998). The neighbourhood data are then transformed into the best-fit plane co-ordinate system, i.e.

$$\begin{bmatrix} u_i \\ v_i \\ w_i \end{bmatrix} = M \left(\begin{bmatrix} x_i \\ y_i \\ z_i \end{bmatrix} - \begin{bmatrix} x_c \\ y_c \\ z_c \end{bmatrix} \right) \quad (2)$$

where (x, y, z) are the scanner-space Cartesian co-ordinates of point i , (u, v, w) are the plane-system co-ordinates and (x_c, y_c, z_c) are the scanner-space co-ordinates of the neighbourhood centroid. Note that the w co-ordinates are simply the residuals from the best-fit plane. The rotation matrix of normalised eigenvectors, M , is obtained from the orthogonal regression procedure.

In the second step a 2D intensity image is resampled from the irregularly-spaced (u, v) co-ordinate data. The pixel spacing is selected to match the nominal point spacing at the target centre. To precisely locate the target centre in the plane, Gaussian first-derivative edge detection filters are convolved with the image. All detected edge points around the circumference of the circle, pictured in Figure 6, are used as observations to determine the centre co-ordinates and radius of the best-fit circle. An equivalent linear form of the circle

model (Förstner and Wrobel, 2004) is used for this. It is important to note that the target image is in fact a circle and not an ellipse since the data acquisition geometry is polar and not perspective. This method of centre location is capable of sub-pixel precision with the following theoretical standard deviation for the pixel spacing Δ

$$\sigma = \pm \frac{\Delta}{\sqrt{12}} \approx 0.289\Delta \quad (3)$$

The inverse of the transformation given by Equation 2 is then applied to the centre co-ordinates of the circle, (u, v) and null w co-ordinate to obtain the scanner-space Cartesian co-ordinates (x, y, z) of the target centre. Spherical co-ordinates (ρ, θ, α) are then derived from these.

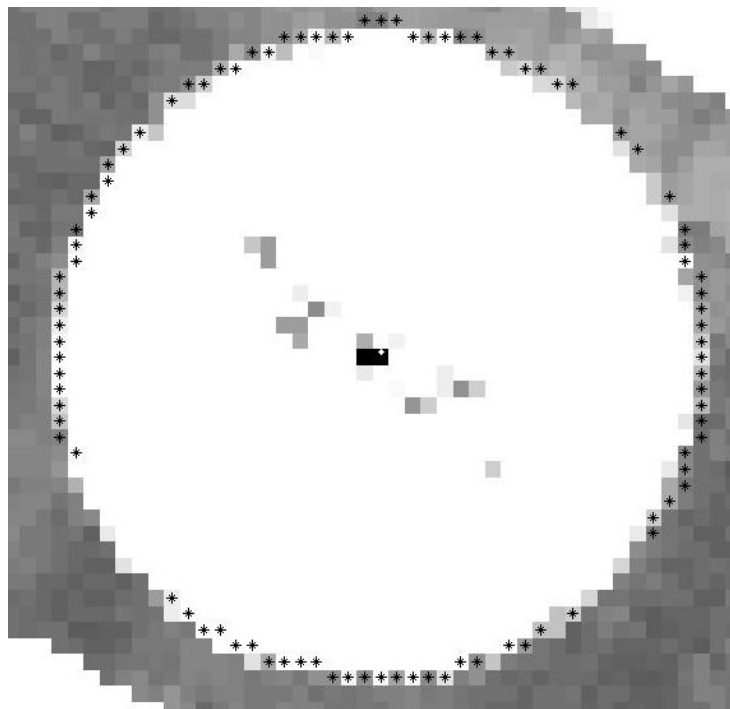


Figure 6. Target image, detected edges (black stars around circumference of circle) and estimated centre (white dot on black background at centre).

Future versions of the software will incorporate a more precise edge detector, such as the moment-preserving method (Mikhail et al., 1984) or, better yet, a least squares fit of a 3D intensity function to the original, non-uniformly spaced data so as to avoid the 2D resampling step.

3. MODELLING AND ESTIMATION

3.1 Self-Calibration Models

The derived observables of range, ρ , horizontal direction, θ , and elevation angle, α , are used in the self-calibration adjustment as it is easier to identify systematic errors from their residuals than it is from those of Cartesian co-ordinates. The observation equations for point I observed in scanner space j are given by

$$\rho_{ij} + v_{\rho_{ij}} = \sqrt{x_{ij}^2 + y_{ij}^2 + z_{ij}^2} + \Delta\rho \quad (4)$$

$$\theta_{ij} + v_{\theta_{ij}} = \arctan\left(\frac{y_{ij}}{x_{ij}}\right) + \Delta\theta \quad (5)$$

$$\alpha_{ij} + v_{\alpha_{ij}} = \arctan\left(\frac{z_{ij}}{\sqrt{x_{ij}^2 + y_{ij}^2}}\right) + \Delta\alpha \quad (6)$$

where

(X_s, Y_s, Z_s) are the object space co-ordinates of scanner position j;

(ω, ϕ, κ) are the Cardan angles (ω, ϕ, κ) for the rotation from object space to scanner space j;

(X, Y, Z) are the object space co-ordinates of object point i;

(x, y, z) are the co-ordinates of object point i in scanner space j; and

R_1, R_2, R_3 are the matrices for rotation about the X-, Y- and Z-axes, respectively.

The rigid body transformation of point i from object space to scanner space j, is given by

$$\begin{aligned} \begin{bmatrix} x_{ij} \\ y_{ij} \\ z_{ij} \end{bmatrix} &= R_3(\kappa_j)R_2(\phi_j)R_1(\omega_j) \left\{ \begin{bmatrix} X_i \\ Y_i \\ Z_i \end{bmatrix} - \begin{bmatrix} X_{s_j} \\ Y_{s_j} \\ Z_{s_j} \end{bmatrix} \right\} \\ &= M_j \left\{ \begin{bmatrix} X_i \\ Y_i \\ Z_i \end{bmatrix} - \begin{bmatrix} X_{s_j} \\ Y_{s_j} \\ Z_{s_j} \end{bmatrix} \right\} \end{aligned} \quad (7)$$

The terms $\Delta\rho$, $\Delta\theta$ and $\Delta\alpha$ represent systematic error correction terms for each observable of the scanner and are assumed to be block-invariant for the purpose of self-calibration. Lichti (2007) develops a full error model for a Faro scanner. For the Surphaser tested in this study, only three additional parameters (APs) were found to be necessary—as will be explained in

detail later—though more can easily be added to the software (some 20 are available at the moment) for future calibrations, if required.

$$\begin{aligned}\Delta\rho &= \varepsilon_{os} + \varepsilon_{int}\alpha_{ij} \\ \Delta\theta &= 0 \\ \Delta\alpha &= \varepsilon_{ecc}\sin(\alpha_{ij})\end{aligned}\tag{8}$$

where ε_{os} is the rangefinder offset or zero error, ε_{int} is an elevation-angle dependent range error that is possibly due to integration time and ε_{ecc} is the error due to vertical circle eccentricity. This cause ε_{int} will be discussed in greater detail in the next sub-section.

3.2 Adjustment Results

The redundancy from the free network, self-calibration adjustment of the Surphaser dataset was 1200 thanks to 1515 observations. Many outliers had to be removed, though, which was done by Baarda's data snooping. Observation weights were optimised by variance component estimation. The identification of the systematic error terms given in Equation 8 was done by exploratory data analysis of the residuals. Figure 7 shows the range residuals as a function of elevation angle for the solution without APs. Note the range of alpha: 0° represents the horizontal position of the collimation axis in front of the instrument and 180° is its horizontal position behind the scanner. Superimposed on Figure 7 is the estimated trend line according to Equation 8. Figure 8 shows the corresponding residual plot for the adjustment case in which the APs of Equation 8 were estimated, which clearly shows that the trend has been removed.

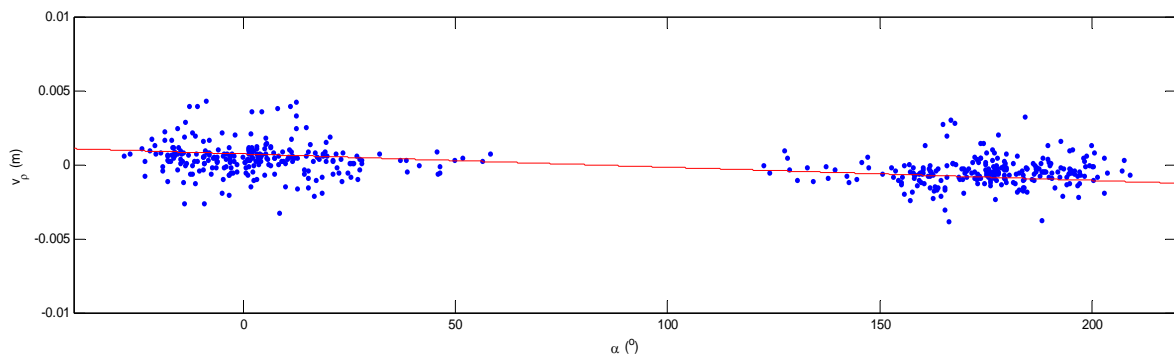


Figure 7. Range residuals as a function of elevation angle for the adjustment case without additional parameters, with estimated trend line superimposed.

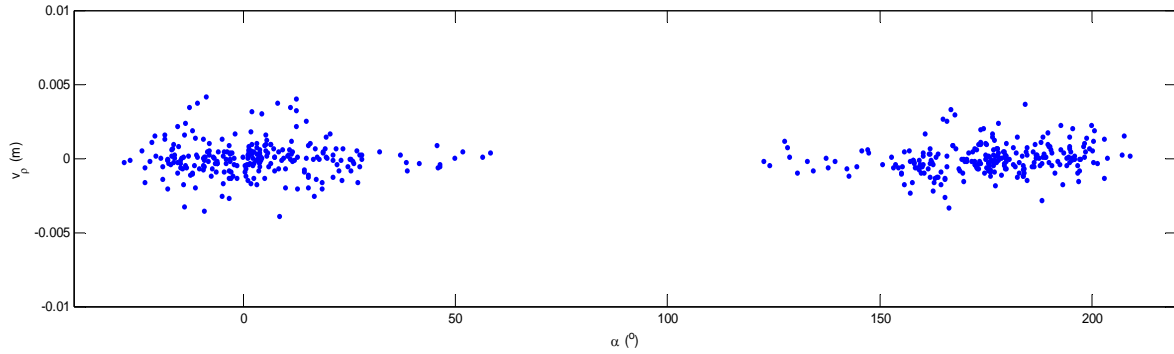


Figure 8. Range residuals as a function of elevation angle for the adjustment case with additional parameters.

Table 1. Estimated APs and their standard deviations

AP	Estimate	σ	Estimate / σ
ϵ_{os} (mm)	-0.7	± 0.2	3.82
ϵ_{int} (mm/° $\times 10^{-3}$)	10	± 0.95	10.62
ϵ_{ecc} (")	58	± 11	5.50

Though the physical significance of the zero and eccentricity errors is clear in both cases, the cause of the systematic error in range as a function of elevation angle is not. It is possibly due to beam travel since during data acquisition the beam moves continuously, even during the integration of return laser energy for a point measurement. It should be noted that the estimated APs are small, as shown in Table 1, (the maximum effect of the combined errors in range is less than 3 mm) but they nonetheless exist and can be precisely estimated thanks to the high redundancy and strong geometry of the self-calibration network design. The figures in the rightmost column of Table 1 show that each AP was statistically significant. No evidence was found of other systematic errors such as collimation and trunnion axis errors, which have been reported in other scanners (e.g., Lichti, 2007; Abmayr et al., 2005).

Presented in Table 2 is the RMS of residuals for each observable group for the cases without and with self-calibration. Only slight improvement is gained by adding the APs, which is expected since there are only three and they are of small magnitude. What is particularly interesting is where the benefit of adding the APs was realised most: in the horizontal direction residuals, which is somewhat counter-intuitive. Improvements to the other variables are marginal or insignificant in terms of RMS, but clear when one inspects the residual plots as exemplified by Figures 7 and 8.

Table 2. RMS of residuals from the adjustments without and with APs.

Observable	RMS (without)	RMS (with)
ρ (mm)	± 1.1	± 1.1
θ (")	± 77.6	± 67.2
α (")	± 49.4	± 49.2

The observation precision estimates from the right-most column of Table 2 differ considerably from the manufacturer's specifications given earlier in this paper. It should be stated, though, that the rangefinder precision of ± 1.1 mm is, however, quite impressive. The elevation angle results are much worse likely due to mass imbalance in the system, which was known to exist in this particular instrument and possibly exacerbated by the photographic tripod that was used (out of necessity) for data capture. Evidence of this effect can be seen in Figure 9, which shows elevation angle residuals as a function of horizontal direction. Note the range of the independent variable is (0° , 180°), which is the range through which the instrument rotates about its vertical axis during data capture. Clearly there is a systematic trend in Figure 9 with zero crossing near 90° . It is important to point out that plots of the same quantities for each individual scan were analysed and the same trend existed in all. This effect could be modelled with, say, a first derivative of Gaussian function that would require three parameters: one for amplitude, one for shape (e.g., variance) and one for offset along the θ -axis.

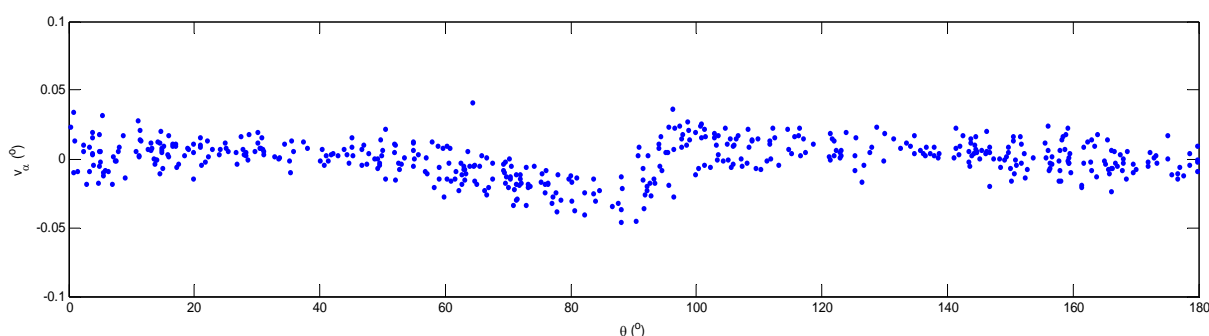


Figure 9. Elevation angle residuals as a function of horizontal direction the adjustment case with additional parameters.

4. CONCLUSIONS

This paper has presented the results of a self-calibration experiment conducted on a Surphaser Hemispherical 3D Scanner 25HS terrestrial laser scanner. A network of signalled point targets was used to perform the calibration Non-linear transformation of the intensity values was found to be necessary prior to target measurement. Results from the calibration show the existence of three sources of systematic error: rangefinder offset, elevation-angle dependent error in range and vertical circle eccentricity. Though the effects of these errors are small, their estimated additional parameters are statistically significant. Evidence of mass imbalance in the system was found in the elevation angle residuals when plotted as a function of horizontal direction.

ACKNOWLEDGEMENTS

The authors gratefully acknowledge the support of Peter Petrov from Basis Software, Inc, USA.

REFERENCES

- Abmayr, T., Dalton, G., Härtl, F., Hines, D., Liu, R., Hirzinger, G., Frölich, C., 2005. Standardization and visualization of 2.5D scanning data and color information by inverse mapping. In: Grün, A., Kahmen, H. (Eds.), *Proceedings Optical 3-D Measurement Techniques VII*, Vienna, Austria, 3-5 October, 2005, Vol. I, pp. 164-173.
- Amiri Parian, J., Grün, A., 2005. Integrated laser scanner and intensity image calibration and accuracy assessment. *The International Archives of the Photogrammetry, Remote Sensing and Spatial Information Sciences* 36 (Part 3/W19), 18-23.
- Basis Software, 2007. http://www.surphaser.com/3dscanner_hs25.html Last accessed 23 January 2007.
- Förstner, W. and Wrobel, B., 2004. Mathematical concepts in photogrammetry. In: McGlone, C. (Ed.) *Manual of Photogrammetry 5th Edition*. ASPRS Bethesda MD. pp 15-180.
- Lichti, D.D., 2007. Modelling, calibration and analysis of an AM-CW terrestrial laser scanner. *ISPRS Journal of Photogrammetry and Remote Sensing*. 61 (5): 307-324.
- Mikhail, E.M., Akey, M.L. and Mitchell, O.R., 1984. Detection and sub-pixel location of photogrammetric targets in digital images, *Photogrammetria*. 39: 63-83
- Reshetyuk, Y., 2006. Calibration of Terrestrial Laser Scanners Callidus 1.1, Leica HDS 3000 and Leica HDS 2500. *Survey Review*, 38 (302): 703-713.
- Shakarji, C. M., 1998. Least-squares fitting algorithms of the NIST algorithm testing system. *Journal of Research of the National Institute of Standards and Technology* 103 (6), 633–641.

BIOGRAPHICAL NOTES

Derek Lichti earned his PhD in Geomatics Engineering from the University of Calgary 1999. Since then he has been with the Department of Spatial Sciences at Curtin University of Technology in Perth, Australia, where he is currently Associate Professor. He is Chair of the ISPRS Working Group V/3 *Terrestrial Laserscanning* for the period 2004-2008. His research interests are in terrestrial laser scanning, airborne laser scanning and close-range metrology.

Jochen Franke, formerly of Curtin University of Technology, is currently Director of Business Development with Scanalyse Pty Ltd located in Perth, Western Australia.

Stefan Brüstle is a full-time student at the University of Karlsruhe, Germany, studying Geodesy and Geoengineering. He is currently working on his Master thesis. He spent two months at the Department of Spatial Sciences at the Curtin University of Technology in Perth to take part in the self-calibration experiment.

CONTACTS

A/Prof Dr Derek Lichti
Department of Spatial Sciences
Curtin University of Technology
GPO Box U1987
Perth, WA 6845
AUSTRALIA
Tel. +61 8 9266 2691
Fax + 61 8 9266 2703
Email: d.lichti@curtin.edu.au
Web site: www.spatial.curtin.edu.au

Stefan Brüstle
Fachschaft Geodäsie
Universität Karlsruhe
Englerstrasse 7
76131 Karlsruhe
Germany
Email: bruste@gik.uni-karlsruhe.de

Jochen Franke
Director of Business Development
Scanalyse Pty Ltd
PO Box 1201, Bentley DC 6983
AUSTRALIA
Tel: +61 8 9355 4426
Fax: +61 8 9355 4422
Email: jochen.franke@scanalyse.com.au
Web site: www.scanalyse.com.au